



**HAL**  
open science

## Electronic properties of rhombohedrally stacked bilayer W Se 2 obtained by chemical vapor deposition

Aymen Mahmoudi, Meryem Bouaziz, Anis Chiout, Gaia Di Berardino, Nathan Ullberg, Geoffroy Kremer, Pavel Dudin, José Avila, Mathieu Silly, Vincent Derycke, et al.

► **To cite this version:**

Aymen Mahmoudi, Meryem Bouaziz, Anis Chiout, Gaia Di Berardino, Nathan Ullberg, et al.. Electronic properties of rhombohedrally stacked bilayer W Se 2 obtained by chemical vapor deposition. *Physical Review B*, 2023, 108 (4), pp.045417. 10.1103/PhysRevB.108.045417 . hal-04302594

**HAL Id: hal-04302594**









**<https://hal.science/hal-04302594v1>**

Submitted on 23 Nov 2023

**HAL** is a multi-disciplinary open access archive for the deposit and dissemination of scientific research documents, whether they are published or not. The documents may come from teaching and research institutions in France or abroad, or from public or private research centers.

L'archive ouverte pluridisciplinaire **HAL**, est destinée au dépôt et à la diffusion de documents scientifiques de niveau recherche, publiés ou non, émanant des établissements d'enseignement et de recherche français ou étrangers, des laboratoires publics ou privés.

## Electronic properties of rhombohedrally stacked bilayer WSe<sub>2</sub> obtained by chemical vapor deposition

Aymen Mahmoudi <sup>1</sup>, Meryem Bouaziz,<sup>1</sup> Anis Chiout,<sup>1</sup> Gaia Di Berardino <sup>1</sup>, Nathan Ullberg <sup>2</sup>, Geoffroy Kremer,<sup>1</sup> Pavel Dudin <sup>3</sup>, José Avila <sup>3</sup>, Mathieu Silly <sup>3</sup>, Vincent Derycke,<sup>2</sup> Davide Romanin <sup>1</sup>, Marco Pala,<sup>1</sup> Iann C. Gerber,<sup>4</sup> Julien Chaste,<sup>1</sup> Fabrice Oehler <sup>1</sup>, and Abdelkarim Ouerghi<sup>1,\*</sup>

<sup>1</sup>Université Paris-Saclay, CNRS, Centre de Nanosciences et de Nanotechnologies, 91120 Palaiseau, France

<sup>2</sup>Université Paris-Saclay, CEA, CNRS, NIMBE, LICSEN, 91191 Gif-sur-Yvette, France

<sup>3</sup>Synchrotron SOLEIL, Université Paris-Saclay, Saint-Aubin, BP48, F91192 Paris, Gif-sur-Yvette, France

<sup>4</sup>Université de Toulouse, INSA-CNRS-UPS, LPCNO, 135 Avenue de Rangueil, 31077 Toulouse, France



(Received 29 March 2023; revised 19 June 2023; accepted 26 June 2023; published 24 July 2023)

Twisted layers of atomically thin two-dimensional materials support a broad range of quantum materials with engineered optical and transport properties. Transition metal dichalcogenides (TMDs) in the rhombohedral ( $3R$ , i.e.,  $0^\circ$  twist) crystal phase have been the focus of significant research interest in optical applications due to their particular broken inversion symmetry. Here, we report experimental and theoretical study of WSe<sub>2</sub> homobilayers obtained in stable  $3R$  configuration by chemical vapor synthesis. We investigate the electronic and structural properties of these  $3R$  WSe<sub>2</sub> bilayers with  $3R$  stacking using micro-Raman spectroscopy, angle-resolved photoemission nanospectroscopy measurements, and density functional theory calculations. Our results demonstrate that WSe<sub>2</sub> bilayers with  $3R$  crystal phase ( $AB$  stacking) show a significant valence-band splitting at the  $K$  point estimated at  $550 \pm 20$  meV. We derived experimentally effective hole masses of  $0.48m_e$  and  $0.73m_e$  at the  $K$  point for upper and lower bands, respectively. Our work opens up perspectives for the development of optoelectronic and spintronic devices based on  $3R$  TMD homobilayers.

DOI: [10.1103/PhysRevB.108.045417](https://doi.org/10.1103/PhysRevB.108.045417)

### I. INTRODUCTION

Two-dimensional (2D) materials, such as graphene [1],  $h$ -BN [2], phosphorene [3], or transition metal dichalcogenides (TMDs) [4], are an ideal platform for studying exciting physical properties not attainable in their bulk counterparts. They exhibit a versatile electronic structure controllable by thickness, surface chemical adsorption, and strain [5,6]. The TMDs family with the  $MX_2$  formula is of particular interest (metal  $M = W, Mo$ , or any other transition metal, and chalcogen  $X = Se, S$ ). They are semiconductors with unique properties in the 2D limit, i.e., when thinned down to single monolayer (ML): direct band gap, large exciton binding energy, well-defined valley degrees of freedom, and wide spin splitting of the valence band [7]. The iconic feature of the TMDs materials family is most certainly the transition from direct to indirect band gap upon increasing thickness, from one to two MLs [8].

Controlling the in-plane crystal arrangement of layered TMD materials is an effective technique to attain exotic physical states [9,10], as observed in the drastically different physical properties between the  $1T$  and  $2H$  phases of TMDs [11,12]. Out of plane, the various stacking possibilities between few layer polytypes are also particularly attractive for piezoelectric applications, valleytronics, photodetectors, or transistors [13–15]. In any bilayer TMD configuration, the weak out-of-plane van der Waals coupling between the

adjacent layers offers a controllable degree of freedom as the (in-plane) twist angle between the top and bottom ML, which is associated with a rich solid state physics [16,17]. Along the continuum, selected twist angles are highly favored energetically and depict the most stable polytypes:  $AA'$  and  $AB$  stacking sequences, also referred to as  $2H$  and  $3R$  bilayer, respectively [18]. For WSe<sub>2</sub>, it has been theoretically predicted that  $AB$  bilayer WSe<sub>2</sub> exhibits different electronic properties compared to the  $AA'$  stacking [18]. More specifically, the rhombohedral-stacked  $3R$  bilayer WSe<sub>2</sub> polytype ( $AB$  stacking) hosts a broken inversion symmetry and may offer perspectives in high efficiency second harmonic generation [15]. Most of the previous studies focus on the “natural”  $2H$  stacking order ( $AA'$ ), i.e., identical to bulk hexagonal WSe<sub>2</sub>, due to the reliance on mechanical exfoliation, whereas the recent advances in synthesis and sequential stacking processes are now allowing the investigation of the more elusive  $3R$  bilayers ( $AB$ ). In particular, these rhombohedral-stacked TMD  $3R$  bilayers have attracted significant interest because of the emergence of an out-of-plane electric polarization from non-ferroelectric monolayer constituents. The bilayer  $3R$  TMD has the polar point group symmetry of  $C_{3v}$  with the polar axis along the  $z$  direction [001]. The  $3R$  homobilayer can be constructed by  $AB$  or  $BA$  stacking sequences, each of which develops a spontaneous electric polarization in the opposite direction of the other [14], leading to ferroelectricity [19] and strong photovoltaic effect [20]. Recent optical studies have shown differences between  $2H$  and  $3R$  stacked WSe<sub>2</sub> bilayers in their photoluminescence (PL) emission, which suggests that the different vertical stacking orders could provide a

\*Corresponding author: [abdelkarim.ouerghi@universite-paris-saclay.fr](mailto:abdelkarim.ouerghi@universite-paris-saclay.fr)

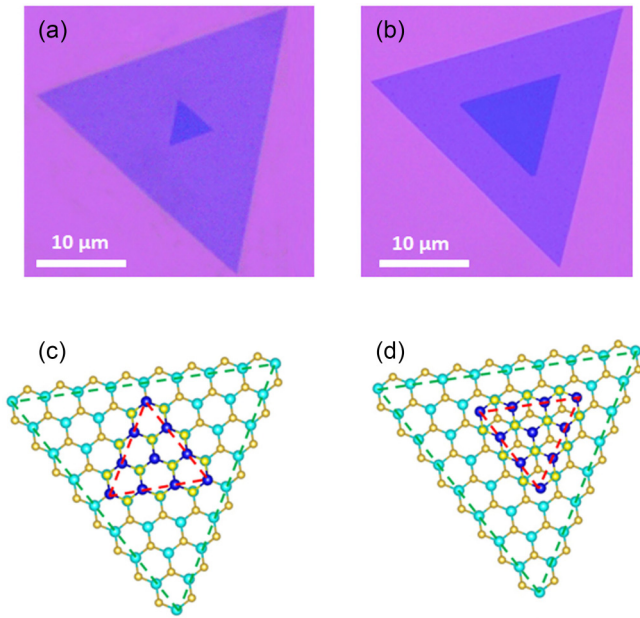


FIG. 1. Optical image of (a) hexagonal  $AA'$  ( $2H$ ) and (b) rhombohedral  $AB$  ( $3R$ )  $WSe_2$  homobilayers, as grown on the  $SiO_2/Si$  substrate. (c),(d) Corresponding atomic arrangements (Se yellow, bottom W cyan, top W blue). The dashed cyan and red lines mark the zigzag Se edges. The  $3R$  configuration is characterized by matching edge orientation between subsequent layers.

way to controllably tune optical properties [21]. However, the impact of stacking order on the complete band structure is not fully addressed. In this context, the direct visualization of the electronic band structure and its correlation with the full crystal structure of bilayer  $3R$   $WSe_2$  using angle-resolved photoemission spectroscopy (ARPES) is very appealing [22]. Nevertheless, in the absence of large-scale samples, it is not possible to separate contributions from areas with different stacking sequence or/and number of layers. To overcome this issue, we use here nano-ARPES to restrict the analysis to nanometric sized regions from well-controlled  $3R$ -bilayer  $WSe_2$  grown using chemical vapor deposition (CVD) [23]. The experimental band structure from nano-ARPES is then compared to theoretical calculations obtained in the density functional theory (DFT) framework. Additional investigations are carried out using micro-PL/Raman spectroscopy and synchrotron-based x-ray photoemission spectroscopy (XPS) for chemical and electronic-structure properties.

## II. RESULT AND DISCUSSION

Bilayer TMDs present two highly energetically favored stacking sequences:  $2H$  ( $AA'$ ) and  $3R$  ( $AB$ ) [18] but the difficulties in fabricating large area  $WSe_2$  bilayer have hindered the analysis of the less stable  $3R$  configuration. Here, we compare the properties of two monocrystalline bilayer  $WSe_2$  with two different stacking orders ( $2H$  and  $3R$ ), which are synthesized during the same chemical CVD experiment (see details in the Methods section). The as-grown  $WSe_2$  crystals are identified on the silica substrate as triangular shaped (50 microns large) whose thickness (1 or 2 MLs) is easily assessed by optical contrast. Optical images in Figs. 1(a) and 1(b)

show respective  $WSe_2$  crystals with ML (light color) and bilayer regions (darker color) in  $2H$  and  $3R$  configurations, characterized by  $60^\circ$  and  $0^\circ$  rotational alignments of the upper  $WSe_2$  layer with respect to the base  $WSe_2$  MLs respectively [15,21,24]. The corresponding atomic configurations are illustrated in Figs. 1(c) and 1(d). In order to confirm the stacking order of the bilayer, we then performed micro-PL and micro-Raman measurements at room temperature.

In Fig. 2, we recorded reference micro-PL spectra of ML  $WSe_2$  and compared it to the two different types of  $WSe_2$  bilayer,  $2H$  and  $3R$ . The type of stacking orders can be deduced directly from the mutual orientation of edges in the first and second  $WSe_2$  layers. The  $3R(AB)$  stacking features parallel edges in both layers, while  $2H(AA')$  stacking has edges rotated by  $60^\circ$  [12,15,21]. An optical image of  $3R$ - $WSe_2$  bilayer is shown Fig. 2(a). The corresponding integrated PL/Raman intensity maps are reported in Figs. 2(b) and 2(c), respectively (see also Supplemental Material S1 [25]). The variations in the intensity contrast in the PL intensity map confirms that the number of layers varies across the flake: a higher PL intensity scale actually indicates a decrease in the number of layers and vice versa. Individual local PL spectra acquired in each region of each flake are shown Figs. 2(d) and 2(e) and confirm this analysis. The 1-ML  $WSe_2$  shows a much higher PL intensity than both types of  $WSe_2$  bilayers, with about a factor of 10 enhancement compared to 2-ML  $WSe_2$  [Fig. 2(d)]. The PL quenching is measured for both  $2H$  and  $3R$  configurations in comparison with the PL of 1 ML. The maximum intensity decreases by  $83 \pm 3\%$  and  $95 \pm 3\%$  for  $2H$  and  $3R$ , respectively. Such large PL quenching at room temperature has been previously reported for many TMD bilayers made by stacking CVD-grown or exfoliated MLs [8,26] and is associated with the indirect band gap transition with increasing ML thickness [7]. Nevertheless, some differences between the  $WSe_2$   $2H$  and  $3R$  bilayers are revealed by PL measurements: the different peak wavelengths (1565 and 1572 meV) and peak full width at half maximum (FWHM, 62 and 44 meV, for the  $3R$  and  $2H$  stacking respectively). For both stacking the stark decrease in intensity indicates that the PL is dominated by momentum-indirect transitions at room temperature, but temperature-dependent measurements are required to study the details of the possible optical transitions [21,24,27].

The corresponding micro-Raman spectra collected at the same position are shown in Fig. 2(e). The observed Raman features are the degenerate in plane  $E'_{2g}$  and out-of-plane  $A_{1g}$  first-order Raman modes around  $247$  and  $249$   $cm^{-1}$ , and the double resonance  $2LA(M)$  mode at  $258$   $cm^{-1}$ . Figure S1 of the Supplemental Material shows integrated Raman maps centered on the  $A_{1g}$  and  $E'_{2g}$  modes of the  $3R$   $WSe_2$  homobilayer on the  $SiO_2/Si$  substrate. The signal is homogeneous over each mono- and bilayer regions. Note that the degeneracy of the  $E'_{2g}$  and  $A_{1g}$  modes, characteristic of  $WSe_2$  1 ML, is fully lifted in the Raman spectra of  $WSe_2$   $3R$  2 ML as shown in Fig. 2(e). The peak at  $308$   $cm^{-1}$ , absent in 1-ML  $WSe_2$ , is the hallmark of thicker 2-ML regions, identical for both the  $2H$  and  $3R$  stackings. For both  $2H$  and  $3R$  bilayers, the  $E'_{2g}$  and  $A_{1g}$  modes now exhibit a  $\sim 2$ - $cm^{-1}$  frequency split, in agreement with theoretical prediction for  $2H$   $WSe_2$  bilayers [28] and experimental reports on  $2H$  and  $3R$   $WSe_2$  homobilayers [29,30]. Due to the change in the crystal structure, the

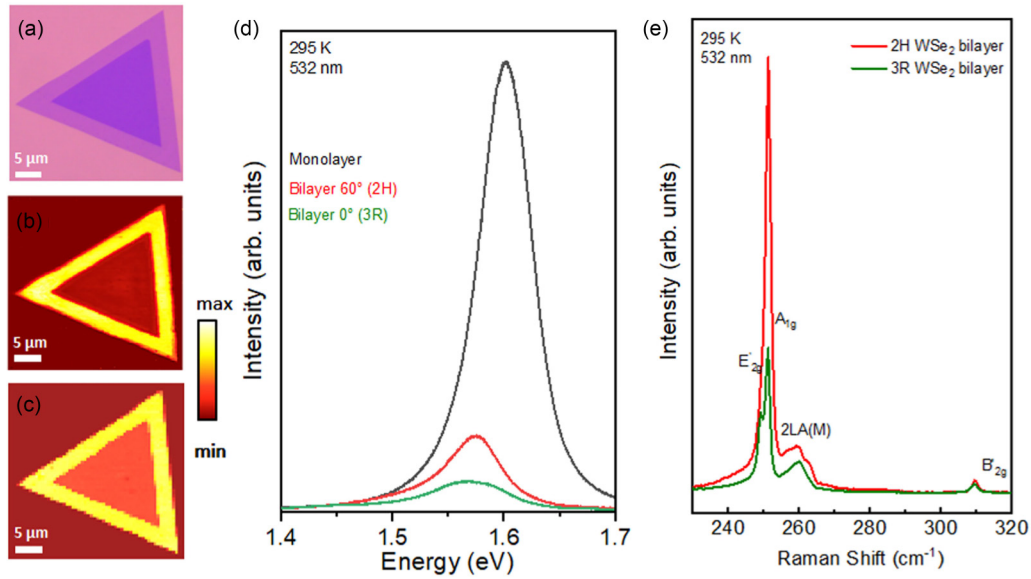


FIG. 2. Structural properties of 3R homobilayer  $\text{WSe}_2/\text{SiO}_2$ : (a) optical image, (b) room temperature micro-PL intensity map. (c) Integrated room temperature micro-Raman map centered on the  $E'_{2g}$  mode of the 3R  $\text{WSe}_2$  bilayer. (d),(e) Comparison of individual micro-PL/Raman spectra acquired in the bilayer regions of 3R and 2H  $\text{WSe}_2$  crystals (532-nm laser).

relative intensity between  $E'_{2g}$  and  $A_{1g}$  are different for room temperature Raman (532-nm laser) and the 3R exhibits a clear  $E'_{2g}$  signal, while it is near absent in the 2H configuration, as reported by others [29,31]. Our DFT calculations show that the frequency splitting is almost the same in both cases (see Fig. S2 of the Supplemental Material). These results confirm that the  $A_{1g}$  mode in the 2H stacking has a Raman signal which is higher by one order of magnitude with respect to the  $E'_{2g}$  one, but this intensity ratio is greatly reduced when moving to the 3R stacking due to symmetry-breaking arguments.

To further characterize the two types of configurations, we carried out optical reflectance measurements. It was previously shown by McCreary *et al.* [29] that the  $\text{WSe}_2$  2H and 3R bilayer have different reflectance spectra. Here, we use wide-field interference reflection microscopy (IRM) to directly measure and compare the reflectance of 2H and 3R  $\text{WSe}_2$  bilayers at multiple wavelengths. In particular, we report in Fig. S3(a) the contrast of  $\text{WSe}_2$  bilayers vs  $\text{WSe}_2$  monolayer for both stacking configurations, in the range  $\lambda = 400\text{--}700$  nm. The contrast difference between 2H and 3R bilayers is most pronounced at  $\lambda = 450$  nm ( $0.21 \pm 0.01$ ) and  $\lambda = 500$  nm ( $0.17 \pm 0.04$ ), while it is minimal at wavelengths above 590 nm. Interestingly, while  $\lambda = 450$  nm yields the highest contrast difference, the case of  $\lambda = 500$  nm is of higher practical interest [see the line profiles and images in Figs. S3(b) and S3(c) respectively], as the reflectivity contrast changes sign between the two configurations. This provides an efficient way to discriminate stacking types in large assemblies of bilayer crystals using wide-field microscopy images acquired at a fixed wavelength.

In order to perform nano-ARPES experiments and to avoid charging effects of our TMD samples during the photoemission process; the CVD-grown  $\text{WSe}_2$  crystals were transferred on a graphene/SiC substrate [30,32] [Fig. 3(a)]. Indeed, graphene is often used as a substrate for TMD heterostructures due to its conductive properties [33]. The transferred 2-ML

$\text{WSe}_2$  flakes were then identified by their optical contrast with respect to the graphene substrate [Fig. 3(b)]. The optical image shows large (lateral size about  $50\ \mu\text{m}$ ) triangular flakes of  $\text{WSe}_2$  on the graphene layer and also confirms the

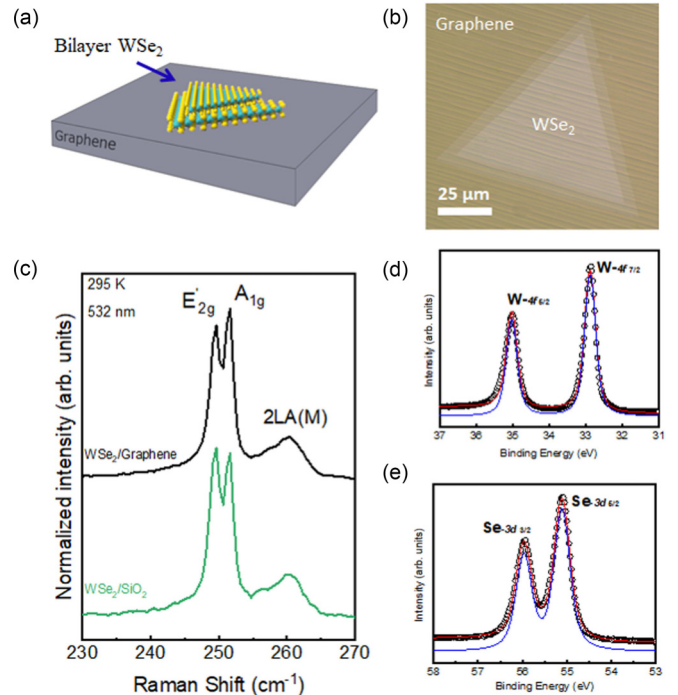


FIG. 3. Structural and electronic properties of bilayer  $\text{WSe}_2/\text{Gr}$  heterostructure: (a) 3D view of  $\text{WSe}_2$  on top of graphene. (b) Optical image of the bilayer  $\text{WSe}_2$  transferred onto the graphene layer; (c) room temperature micro-Raman spectra of bilayer before transfer (2-ML  $\text{WS}_2/\text{SiO}_2$ ; green line), and after transfer (2-ML  $\text{WS}_2/\text{graphene}$ ; black line); (d),(e) XPS spectra of W-4f and Se-3d core levels recorded in the bilayer region of sample in panel (b).

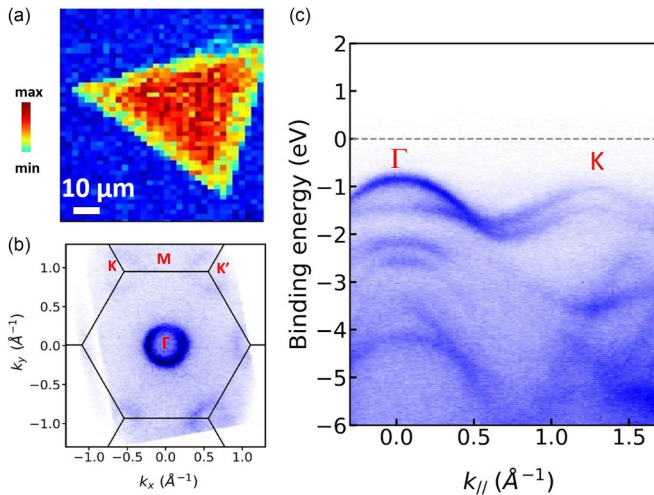


FIG. 4. (a) Spatially resolved ARPES map of the bilayer 3R-WSe<sub>2</sub> sample; (b) isoenergy cut in the  $\Gamma K$  plane obtained in surface-sensitive conditions ( $h\nu = 100$  eV) at  $-2$  eV binding energy, (c) high resolution map of the electronic band structure of bilayer WSe<sub>2</sub> collected at  $h\nu = 100$  eV and  $T = 70$  K along the  $K\Gamma$  high-symmetry direction.

absence of large-scale damage which could be a consequence of the transfer process. Each stripe on the optical image is attributed to an atomic step on the SiC(0001) substrate [34]. In Fig. 3(c), we confirm that micro-Raman spectra of WSe<sub>2</sub>/SiO<sub>2</sub> and WSe<sub>2</sub>/graphene substrate are similar before and after the transfer to the graphene substrate (Fig. 2), which further confirms the absence of any structural damage during the transfer process. Chemical analysis by XPS is shown in Fig. 3(d), with W-4*f* and Se-2*p* XPS peaks deconvolution. The W component of WSe<sub>2</sub> is well fitted by a doublet peak at binding energy (BE) of 33.4 and 35.6 eV, corresponding to W-4*f*<sub>7/2</sub> and W-4*f*<sub>5/2</sub> core energy levels, respectively. The selenium Se-3*d* peak consists of a single doublet (Se-3*d*<sub>5/2</sub> at BE = 55 eV and Se-3*d*<sub>3/2</sub> at BE = 56 eV) corresponding to Se-W bonding, and validates the stoichiometry of WSe<sub>2</sub>. The absence of any oxygen O-2*p* signal with binding energy around 5–10 eV marks the high quality of the interface between the WSe<sub>2</sub> and the graphene layer.

We now turn our attention to the electronic structure of the above described 3R-bilayer WSe<sub>2</sub>. To do so, we have performed nano-ARPES measurements at the ANTARES beamline of the synchrotron SOLEIL at low temperature (70 K), with a spatial resolution of 600 nm. For this XPS measurement, the conductivity of the substrate is important to avoid the electronic charging of the film during the XPS/ARPES. Graphene/SiC(0001) may be a suitable material to combine with TMD due to its lack of dangling bonds and chemical inertness. In order to limit any charge transfer between the bilayer WSe<sub>2</sub> and graphene substrate, we have used the 3–4 layer of graphene/SiC, for which the Dirac point is located at the Fermi level [22]. In Fig. 4(a) we show the angle and energy integrated photoemission map coming from the 3R-WSe<sub>2</sub> bilayer crystal shown in Fig. 3(b). The photoemission intensity around the  $\Gamma$  point was acquired along the  $\Gamma K$  direction for a photon energy  $h\nu = 100$  eV as a function

of coordinate on surface [35]. The mono- and bilayer regions of the flake can be directly identified as low and high intensity areas on the integrated intensity map, and match the data obtained by optical microscopy or Raman analysis. The large and homogeneous over surface intensity confirms the uniform thickness of the 2-ML region. Figure 4(b) presents an isoenergy cut obtained at BE =  $-2$  eV binding energy of the 3R-WSe<sub>2</sub> BL (*AB* stacking). We have chosen this particular binding energy in order to highlight the valence-band maximum (VBM) dispersions both at the  $K$  and  $\Gamma$  points of the Brillouin zone (BZ). We observe a circular (isotropic) hole pocket at the  $\Gamma$  point and a triangular hole pocket at each  $K$  point which is typical for the hexagonal WSe<sub>2</sub> 2-ML crystals. The presence of a unique set of six pockets at well-determined  $K$  positions in the reciprocal lattice confirms that the WSe<sub>2</sub> crystal is of a single domain (i.e., monocrystal).

The energy-momentum cut along the high-symmetry  $\Gamma K$  direction of 3R-WSe<sub>2</sub> bilayer is shown Fig. 4(c). From the experimental  $\Gamma K$  spectrum, we can evaluate the number of branches at the  $\Gamma$  point, the energy position of the valence-band maximum (VBM), and the valence-band splitting at the  $K$  point of the band structure. We first note the presence of two separated bands near the  $\Gamma$  point confirming the band structure to originate from the 3R-bilayer region (2 MLs, *AB*). The energy difference between the Fermi level ( $E_F$ ) and the VBM is approximately equal to 0.7 eV. Considering the optical band-gap energy (1.57 eV) of bilayer 3R WSe<sub>2</sub> determined in Fig. 2(b), we can conclude that our sample is hole doped, since the VBM is closer to  $E_F$  compared to the conduction-band minimum (CBM). This observation persists in the 1-ML region (not shown) and consequently suggests that the observed *p*-type character possibly relates to the growth conditions [36]. We have also fitted the experimental dispersions in the vicinity ( $\pm 0.12^\circ \text{ \AA}^{-1}$ ) of the  $K$  point using a parabolic approximation in order to extract the effective mass values of the hole's bands. The experimental dispersion has been fitted with a parabolic model  $E(k) = E + \hbar k^2/2m^*$  where  $m^*$  is the effective electron mass and  $\hbar$  is the reduced Planck. We find  $m^* = 0.48m_e$  for the low energy band and  $m^* = 0.73m_e$  for the high energy band. The observed splitting of the valence band along the  $\Gamma K$  direction of our 3R bilayer WSe<sub>2</sub> is due to the strong spin-orbit coupling originating from the high mass of the constituent elements and the lack of inversion symmetry [37,38].

To better understand the band structure as well as the specificities of the 3R-WSe<sub>2</sub> 2-ML configuration, we have performed out band structure calculations using DFT with the hybrid functional HSE06. We were also able to compare them with previous calculations at the  $G_0W_0$  level, to consider many-body effects, already reported in Ref. [31]. It is known that the more symmetrical 2*H* configuration shows two energetically degenerate bands near the  $K$  points, while the 3*R* stacking presents four different bands ( $k = 1.2 \text{ \AA}^{-1}$ ) [21]. The band structure of 3*R* bilayer thus presents different transition energies at the  $K$  point. This is in contrast to 2*H* stacking, where both MLs, and their associate intralayer states, are energetically degenerate [21]. Comparing with the experimental data for a monolayer of WSe<sub>2</sub> or WS<sub>2</sub> [39,40], we see an overall broadening (30 meV) of the band structure at the  $K$  point. The upper and lower bands are theoretically

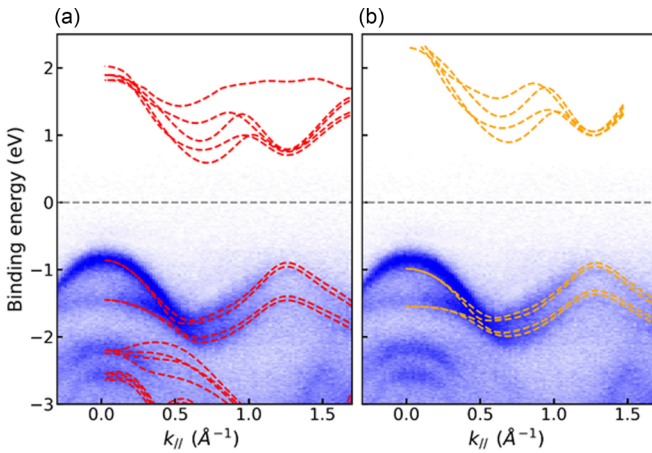


FIG. 5. Comparison between experimental and theoretical band structure of 3R homobilayer WSe<sub>2</sub>. (a) HSE06 DFT (red) calculation for the present work. (b)  $G_0W_0$  (yellow) taken from Ref. [31].

split by about 21 meV, which is larger than our experimental energy resolution and thus should have been resolved directly in our measurements. However, we do not clearly resolve four individual bands in the vicinity of  $K$ , only an increasing linewidth of the band structure in the direction of  $\Gamma K$ , which we attribute here to 3R-specific bands splitting. We conjecture that the sample roughness, induced in the growth or transfer process, does not allow for the full band structure determination at the nominal energy resolution. Figures 5(a) and 5(b) show the measured band structure and the calculated occupied states using HSE06. The distinctive features of band structure include the VBM at  $\Gamma$  (derived from the W  $d_{z^2}$  and Se  $p_z$  orbitals), the VBM at  $K$  (W  $d_{x^2-y^2}/d_{xy}$  and Se  $p_x/p_y$  orbitals) and the valley between  $\Gamma$  and  $K$  (crossover from W  $d_{z^2}$  and Se  $p_z$  to W  $d_{x^2-y^2}/d_{xy}$  orbitals) [32]. Supplemental Material Fig. S4 shows the EDCs profiles spectra at the  $K$  and  $\Gamma$  points with a Gaussian fit to estimate the splitting values. The valence-band splitting at the  $K$  point is about  $550 \pm 20$  meV and the splitting at the  $\Gamma$  point is about  $620 \pm 20$  meV. Those values agree with those calculated from the DFT calculations from the HSE06 and  $G_0W_0$  correction, Figs. 5(a) and 5(b). The main difference between HSE06 and  $G_0W_0$  calculations resides in the VBM: when HSE06 locates the maximum in  $\Gamma$ , by more than 40 meV with respect to the maximum in  $K$ , the  $G_0W_0$  scheme provides the VBM in  $K$  by more than 100 meV. We recall that those energy differences are highly sensitive to lattice parameter and exchange-correlation functional choices as discussed previously for TMD monolayers [41], which can also be the case experimentally due to strain effect [42] in bilayer systems, for instance. The spin polarization of the depicted bands is shown in Fig. S5. We observe that the two highest VBMs possess the same spin state at  $K$  (spin down in red) while the next two lowest are of the opposite spin (spin up in black). This is directly linked to the 3R crystal structure and each pair of bands (spin up + down) corresponds to one of the two distinct WSe<sub>2</sub> layers. In the conduction band (CB), the energy ordering at  $K$  is different with spin up and down bands from the first layer, and then spin up and down from the second layer at slightly higher energy. The difference between CB and VB band ordering at  $K$  is due to a much

smaller spin splitting in CB, combined with a high degree of localization of those states, which corresponds to a weak hybridization between the layers. In the  $Q$  valley, the spin polarization is globally weaker, with a much stronger mixing of states between the two layers, but it remains sizable and leads to a distinct ordering of spin in the CBs.

In summary, we have successfully studied the growth and the electronic structure of a 3R stacked bilayer WSe<sub>2</sub>. A minor PL quenching and peak shift were observed for the 3R WSe<sub>2</sub> bilayer structure with respect to the 2H stacking. By performing nano-ARPES experiments, we have spatially mapped the electronic band structure of 3R WSe<sub>2</sub> bilayer. We observed sharp ARPES bands, in particular for the VBM near the  $\Gamma$  and  $K$  points. We directly observed the strong valence-band splitting at the  $k$  point and its value is in good agreement with the DFT calculations. We have further extracted the effective masses at the  $K$  point of the BZ, finding hole effective mass of  $0.48m_e$  (upper band) and  $0.73m_e$  (lower band). The valence-band splitting of the VB at  $K$  is experimentally determined to  $550 \pm 20$  meV. Our results provide a starting point for future studies of electronic properties of WSe<sub>2</sub> bilayers and their applications in spintronic and valleytronic devices.

### III. METHODS

WSe<sub>2</sub> crystals were grown by chemical vapor deposition (CVD) in a customized 4 inch. Nabertherm (RST 120) horizontal oven on SiO<sub>2</sub>/Si substrates [283-nm thick SiO<sub>2</sub> on Si(100), Nova Wafers]. Argon (Ar, 200 sccm) and hydrogen (H<sub>2</sub>, 10 sccm) are used as carrier gases; the pressure is 2.5 mbar for the whole growth procedure. The actual growth duration at high temperature is 30 min, excluding the temperature ramps from and to room temperature (60 min ramp up, 120 min ramp down). During growth, the selenium source is elemental Se (Neyco 99.9%) contained in a quartz crucible heated at 250° C. The tungsten source is H<sub>2</sub>WO<sub>4</sub> (Acros Organics, 99%) mixed with KCl (Alfa Aesar, 99.9%) powder heated to 850° C, placed upstream to SiO<sub>2</sub>/Si substrates. Both 3R and 2H bilayers are found over the SiO<sub>2</sub>/Si substrate (5 × 2 cm), with an overwhelming fraction of 3R homobilayers compared to 2H stacking, in line with other experimental reports using comparable substrate temperature [15]. Graphene on 4H-SiC(0001) is used as conductive host substrate during the ARPES investigations, produced via a two-step process in another CVD system [43]. Prior to graphitization, the substrate was hydrogen etched (100% H<sub>2</sub>) at 1550° C to produce well-ordered atomic terraces of SiC [34]. Subsequently, the SiC sample was heated to 1000° C and then further heated to 1550° C in an Ar atmosphere to obtain the desired single layer graphene. For the transfer process PMMA was spin coated onto the WSe<sub>2</sub> flakes and peeled them off from the SiO<sub>2</sub> substrate by wet etching in KOH solution. Afterward, the PMMA/WSe<sub>2</sub> layer was transferred onto the conductive graphene/SiC substrate. The PMMA was finally removed using acetone. After the transfer of WSe<sub>2</sub> onto graphene, an annealing process at  $T = 300^\circ \text{C}$  for 30 min in UHV (base pressure better than  $P \sim 10^{-10}$  mbar) was used to further clean the surface and interface of the WSe<sub>2</sub> graphene heterostructure. The shape of the flakes and their huge size was not modified after the transfer [44].

Micro-Raman spectroscopy measurements were conducted at room temperature using a Horiba Labram Raman spectrometer operating at laser of wavelength  $\lambda = 532$  nm. The ARPES experiments were performed at the ANTARES beamline of the SOLEIL synchrotron light source (Saint-Aubin, France). The ARPES data were taken at a photon energy of 95 eV, using linearly polarized light. All ARPES measurements were carried out at a pressure of  $10^{-11}$  mbar and at a temperature of 70 K. The band positions were determined by energy curve analysis (EDC) of the ARPES spectra as reported in the Supplemental Material [25]. Spin projected band structure calculation of 3R WSe<sub>2</sub> homobilayer and IRM measurements of 3R and 2H bilayer WSe<sub>2</sub> are also shown, as well as are Raman active frequencies and phonon dispersions of 2H and 3R WSe<sub>2</sub> homobilayers.

Density functional theory (DFT) calculations were performed using the VASP package [45] using the projector augmented wave formalism [25,46,47] to tackle the core electrons issue. Fourteen electrons for W atoms and six for Se ones were explicitly included in the valence states. A grid of  $12 \times 12 \times 1$   $k$  points has been used in conjunction with a Gaussian smearing of 0.05 eV of width for partial occupancies. The bilayer WSe<sub>2</sub> in-plane lattice parameter was fixed to 3.32 Å with a vacuum height of 21.6 Å between periodic images in the  $z$  direction, to reduce spurious interaction. The first optimization process of the geometry was performed at the PBE-D3 level [25,48] to include van der Waals interac-

tion between layers and then the Heyd-Scuseria-Ernzerhof (HSE06) hybrid functional [25,49–51] was used as an approximation of the exchange-correlation electronic term, to obtain a reliable band structure after a Wannier interpolation procedure performed with the WANNIER90 program [52].

The data sets generated during and/or analyzed during the current study are available from the corresponding author on reasonable request.

## ACKNOWLEDGMENTS

We acknowledge the financial support by MagicValley (Grant No. ANR-18-CE24-0007), 2D-on-demand project (Grant No. ANR-20-CE09-0026) and Graskop (Grant No. ANR-19-CE09-0026) grants. This work was also supported by a public grant overseen by the French National Research Agency (ANR) as part of the “Investissements d’Avenir” program (Labex NanoSaclay, Grant No. ANR-10-LABX-0035) and by the French technological network RENATECH. I.C.G. acknowledges the CALMIP initiative for the generous allocation of computational time, through Project No. p0812, as well as GENCI-TGCC and GENCI-IDRIS for Grant No. A012096649. D.R. acknowledges GENCI-TGCC and GENCI-IDRIS for Grant No. A0140914101.

There are no conflicts to declare.

- 
- [1] A. K. Geim, Graphene: Status and prospects, *Science* **324**, 1530 (2009).
- [2] T. Q. P. Vuong, G. Cassabois, P. Valvin, A. Ouerghi, Y. Chassigneux, C. Voisin, and B. Gil, Phonon-Photon Mapping in A Color Center In Hexagonal Boron Nitride, *Phys. Rev. Lett.* **117**, 097402 (2016).
- [3] J. Shim, S. Oh, D. H. Kang, S. H. Jo, M. H. Ali, W. Y. Choi, K. Heo, J. Jeon, S. Lee, M. Kim *et al.*, Phosphorene/rhenium disulfide heterojunction-based negative differential resistance device for multi-valued logic, *Nat. Commun.* **7**, 13413 (2016).
- [4] K. F. Mak, K. He, J. Shan, and T. F. Heinz, Control of valley polarization in monolayer MoS<sub>2</sub> by optical helicity, *Nat. Nanotechnol.* **7**, 494 (2012).
- [5] S. B. Desai, G. Seol, J. S. Kang, H. Fang, C. Battaglia, R. Kapadia, J. W. Ager, J. Guo, and A. Javey, Strain-induced indirect to direct bandgap transition in multilayer WSe<sub>2</sub>, *Nano Lett.* **14**, 4592 (2014).
- [6] J. Chaste, A. Missaoui, S. Huang, H. Henck, Z. Ben Aziza, L. Ferlazzo, C. Naylor, A. Balan, A. T. C. Johnson, R. Braive *et al.*, Intrinsic properties of suspended MoS<sub>2</sub> on SiO<sub>2</sub>/Si pillar arrays for nanomechanics and optics, *ACS Nano* **12**, 3235 (2018).
- [7] N. Alidoust, G. Bian, S. Y. Xu, R. Sankar, M. Neupane, C. Liu, I. Belopolski, D. X. Qu, J. D. Denlinger, F. C. Chou *et al.*, Observation of monolayer valence band spin-orbit effect and induced quantum well states in MoX<sub>2</sub>, *Nat. Commun.* **5**, 4673 (2014).
- [8] Y. Zhang, T. R. Chang, B. Zhou, Y. T. Cui, H. Yan, Z. Liu, F. Schmitt, J. Lee, R. Moore, Y. Chen *et al.*, Direct observation of the transition from indirect to direct bandgap in atomically thin epitaxial MoSe<sub>2</sub>, *Nat. Nanotechnol.* **9**, 111 (2014).
- [9] M. M. Ugeda, A. Pulkin, S. Tang, H. Ryu, Q. Wu, Y. Zhang, D. Wong, Z. Pedramrazi, A. Martín-Recio, Y. Chen *et al.*, Observation of topologically protected states at crystalline phase boundaries in single-layer WSe<sub>2</sub>, *Nat. Commun.* **9**, 3401 (2018).
- [10] P. Chen, W. W. Pai, Y.-H. Chan, W.-L. Sun, C.-Z. Xu, D.-S. Lin, M. Y. Chou, A.-V. Fedorov, and T.-C. Chiang, Large quantum-spin-hall gap in single-layer 1T' WSe<sub>2</sub>, *Nat. Commun.* **9**, 2003 (2018).
- [11] A. Ambrosi, Z. Sofer, and M. Pumera, 2H → 1T phase transition and hydrogen evolution activity of MoS<sub>2</sub>, MoSe<sub>2</sub>, WS<sub>2</sub> and WSe<sub>2</sub> strongly depends on the MX<sub>2</sub> composition, *Chem. Commun.* **51**, 8450 (2015).
- [12] S. M. Shinde, K. P. Dhakal, X. Chen, W. S. Yun, J. Lee, H. Kim, and J.-H. Ahn, Stacking-controllable interlayer coupling and symmetric configuration of multilayered Mos<sub>2</sub>, *ngp Asia Mater.* **10**, e468 (2018).
- [13] Z. Zhang, Y. Wang, K. Watanabe, T. Taniguchi, K. Ueno, E. Tutuc, and B. J. LeRoy, Flat bands in twisted bilayer transition metal dichalcogenides, *Nat. Phys.* **16**, 1093 (2020).
- [14] L. Wang, E. M. Shih, A. Ghiotto, L. Xian, D. A. Rhodes, C. Tan, M. Claassen, D. M. Kennes, Y. Bai, B. Kim *et al.*, Correlated electronic phases in twisted bilayer transition metal dichalcogenides, *Nat. Mater.* **19**, 861 (2020).
- [15] Z. Zeng, X. Sun, D. Zhang, W. Zheng, X. Fan, M. He, T. Xu, L. Sun, X. Wang, and A. Pan, Controlled vapor growth and nonlinear optical applications of large-area 3R Phase WS<sub>2</sub> and WSe<sub>2</sub> atomic layers, *Adv. Funct. Mater.* **29**, 1806874 (2019).
- [16] K. Liu, L. Zhang, T. Cao, C. Jin, D. Qiu, Q. Zhou, A. Zettl, P. Yang, S. G. Louie, and F. Wang, Evolution of interlayer

- coupling in twisted molybdenum disulfide bilayers, *Nat. Commun.* **5**, 4966 (2014).
- [17] M. H. Naik and M. Jain, Ultraflatbands and Shear Solitons in Moiré Patterns of Twisted Bilayer Transition Metal Dichalcogenides, *Phys. Rev. Lett.* **121**, 266401 (2018).
- [18] J. He, K. Hummer, and C. Franchini, Stacking effects on the electronic and optical properties of bilayer transition metal dichalcogenides MoS<sub>2</sub>, MoSe<sub>2</sub>, WS<sub>2</sub>, and WSe<sub>2</sub>, *Phys. Rev. B* **89**, 075409 (2014).
- [19] J. Liang, D. Yang, J. Wu, J. I. Dadap, K. Watanabe, T. Taniguchi, and Z. Ye, Optically Probing the Asymmetric Interlayer Coupling in Rhombohedral-Stacked MoS<sub>2</sub> Bilayer, *Phys. Rev. X* **12**, 041005 (2022).
- [20] J. Wu, D. Yang, J. Liang, M. Werner, E. Ostroumov, Y. Xiao, K. Watanabe, T. Taniguchi, J. I. Dadap, D. Jones *et al.*, Ultrafast response of spontaneous photovoltaic effect in 3R-MoS<sub>2</sub>-based heterostructures, *Sci. Adv.* **8**, eade3759 (2022).
- [21] I. Paradisanos, S. Shree, A. George, N. Leisgang, C. Robert, K. Watanabe, T. Taniguchi, R. J. Warburton, A. Turchanin, X. Marie *et al.*, Controlling interlayer excitons in MoS<sub>2</sub> layers grown by chemical vapor deposition, *Nat. Commun.* **11**, 2391 (2020).
- [22] D. Pierucci, H. Sediri, M. Hajlaoui, J. Girard, T. Brumme, M. Calandra, E. Velez-fort, G. Patriarche, M. G. Silly, G. Ferro *et al.*, Evidence for flat bands near the fermi level in epitaxial rhombohedral multilayer graphene, *ACS Nano* **9**, 5432 (2015).
- [23] J. Zribi, L. Khalil, B. Zheng, J. Avila, D. Pierucci, T. Brulé, J. Chaste, E. Lhuillier, M. C. Asensio, A. Pan *et al.*, Strong interlayer hybridization in the aligned SnS<sub>2</sub>/WSe<sub>2</sub> hetero-bilayer structure, *npj 2D Mater. Appl.* **3**, 27 (2019).
- [24] X. Li, X. Shi, D. Marian, D. Soriano, T. Cusati, G. Iannaccone, G. Fiori, Q. Guo, W. Zhao, and Y. Wu, Rhombohedral-stacked bilayer transition metal dichalcogenides for high-performance atomically thin CMOS devices, *Sci. Adv.* **9**, eade5706 (2023).
- [25] See Supplemental Material at <http://link.aps.org/supplemental/10.1103/PhysRevB.108.045417> for the methods used in the first-principles calculations, modeling configurations of the bilayer structure, employed Perdew-Burke-Ernzerhof exchange-correlation functional, and type of used pseudopotential.
- [26] K. F. Mak, C. Lee, J. Hone, J. Shan, and T. F. Heinz, Atomically Thin MoS<sub>2</sub>: A New Direct-Gap Semiconductor, *Phys. Rev. Lett.* **105**, 136805 (2010).
- [27] R. H. Godiksen, S. Wang, T. V. Raziman, J. G. Rivas, and A. G. Curto, Impact of indirect transitions on valley polarization in WS<sub>2</sub> and WSe<sub>2</sub>, *Nanoscale* **14**, 17761 (2022).
- [28] H. Terrones, E. Del Corro, S. Feng, J. M. Poumirol, D. Rhodes, D. Smirnov, N. R. Pradhan, Z. Lin, M. A. T. Nguyen, A. L. Elías *et al.*, New first order raman-active modes in few layered transition metal dichalcogenides, *Sci. Rep.* **4**, 4215 (2014).
- [29] K. M. McCreary, M. Phillips, H. J. Chuang, D. Wickramaratne, M. Rosenberger, C. S. Hellberg, and B. T. Jonker, Stacking-dependent optical properties in bilayer WSe<sub>2</sub>, *Nanoscale* **14**, 147 (2022).
- [30] D. Pierucci, H. Henck, J. Avila, A. Balan, C. H. Naylor, Y. J. Dappe, M. G. Silly, F. Sirotti, A. T. C. Johnson, M. C. Asensio *et al.*, Band alignment and minigaps in monolayer MoS<sub>2</sub>-graphene van der waals heterostructures, *Nano Lett.* **16**, 4054 (2016).
- [31] Z. Li, J. Förste, K. Watanabe, T. Taniguchi, B. Urbaszek, A. S. Baimuratov, I. C. Gerber, A. Högele, and I. Bilgin, Stacking-dependent exciton multiplicity in WSe<sub>2</sub> bilayers, *Phys. Rev. B* **106**, 045411 (2022).
- [32] C. Ernan-des, L. Khalil, H. Almabrouk, D. Pierucci, B. Zheng, J. Avila, P. Dudin, J. Chaste, F. Oehler, M. Pala *et al.*, Indirect to direct band gap crossover in two-dimensional WS<sub>2(1-x)</sub>Se<sub>2x</sub> alloys, *npj 2D Mater. Appl.* **5**, 7 (2021).
- [33] H. Henck, D. Pierucci, Z. Ben Aziza, M. G. Silly, B. Gil, F. Sirotti, G. Cassabo-is, and A. Ouerghi, Stacking fault and defects in single domain multilayered hexagonal boron nitride, *Appl. Phys. Lett.* **110**, 023101 (2017).
- [34] E. Pallecchi, F. Lafont, V. Cavaliere, F. Schopfer, D. Maily, W. Poirier, and A. Ouerghi, High electron mobility in epitaxial graphene on 4H-SiC(0001) via post-growth annealing under hydrogen, *Sci. Rep.* **4**, 4558 (2014).
- [35] H. Henck, J. Avila, Z. Ben Aziza, D. Pierucci, J. Baima, B. Pamuk, J. Chaste, D. Utt, M. Bartos, K. Nogajewski *et al.*, Flat electronic bands in long sequences of rhombohedral-stacked graphene, *Phys. Rev. B* **97**, 245421 (2018).
- [36] D. Pierucci, A. Mahmoudi, M. Silly, F. Bisti, F. Oehler, G. Patriarche, F. Bonell, A. Marty, C. Vergnaud, M. Jamet *et al.*, Evidence for highly P-type doping and type ii band alignment in large scale monolayer WSe<sub>2</sub>/Se-terminated GaAs heterojunction grown by molecular beam epitaxy, *Nanoscale* **14**, 5859 (2022).
- [37] N. R. Wilson, P. Rivera, A. J. Marsden, N. D. M. Hine, P. V. Nguyen, G. C. Constantinescu, N. R. Wilson, V. Kandyba, D. H. Cobden, K. Seyler *et al.*, Determination of band offsets, hybridization, and exciton binding in 2D semiconductor heterostructures, *Sci. Adv.* **3**, e1601832 (2017).
- [38] Y. Zhang, M. M. Ugeda, C. Jin, S. F. Shi, A. J. Bradley, A. Martín-Recio, H. Ryu, J. Kim, S. Tang, Y. Kim *et al.*, Electronic structure, surface doping, and optical response in epitaxial WSe<sub>2</sub> thin films, *Nano Lett.* **16**, 2485 (2016).
- [39] J. Zribi, D. Pierucci, F. Bisti, B. Zheng, J. Avila, L. Khalil, C. Ernan-des, J. Chaste, F. Oehler, M. Pala, T. Maroutian, I. Hermes, E. Lhuillier, A. Pan, and A. Ouerghi, Unidirectional Rashba spin splitting in single layer WS<sub>2(1-x)</sub>Se<sub>2x</sub> alloy, *Nanotechnology* **34**, 075705 (2023).
- [40] H. Henck, Z. Ben Aziza, D. Pierucci, F. Laourine, F. Reale, P. Palczynski, J. Chaste, M. G. Silly, F. Bertran, P. Le Fèvre *et al.*, Electronic band structure of two-dimensional WS<sub>2</sub>/Graphene van Der Waals heterostructures, *Phys. Rev. B* **97**, 155421 (2018).
- [41] J. P. Echeverry, B. Urbaszek, T. Amand, X. Marie, and I. C. Gerber, Splitting between bright and dark excitons in transition metal dichalcogenide monolayers, *Phys. Rev. B* **93**, 121107 (2016).
- [42] O. B. Aslan, M. Deng, M. L. Brongersma, and T. F. Heinz, Strained bilayer WSe<sub>2</sub> with reduced exciton-phonon coupling, *Phys. Rev. B* **101**, 115305 (2020).
- [43] J. Penuelas, A. Ouerghi, D. Lucot, C. David, J. Gierak, H. Estrade-Szwarczkopf, and C. Andreazza-Vignolle, Surface Morphology and characterization of thin graphene films on SiC vicinal substrate, *Phys. Rev. B* **79**, 033408 (2009).
- [44] C. Ernan-des, L. Khalil, H. Henck, M.-Q. Zhao, J. Chaste, F. Oehler, A. T. Charlie Johnson, M. C. Asensio, D. Pierucci, M. Pala *et al.*, Strain and spin-orbit coupling engineering in



- twisted WS<sub>2</sub>/graphene heterobilayer, *Nanomaterials* **11**, 2921 (2021).
- [45] G. Kresse and J. Furthmüller, Efficient iterative schemes for ab initio total-energy calculations using a plane-wave basis set, *Phys. Rev. B* **54**, 11169 (1996).
- [46] P. E. Blöchl, Projector augmented-wave method, *Phys. Rev. B* **50**, 17953 (1994).
- [47] G. Kresse and D. Joubert, From ultrasoft pseudopotentials to the projector augmented-wave method, *Phys. Rev. B* **59**, 1758 (1999).
- [48] S. Grimme, J. Antony, S. Ehrlich, and H. Krieg, A consistent and accurate ab initio parametrization of density functional dispersion correction (DFT-D) for the 94 elements H-Pu, *J. Chem. Phys.* **132**, 154104 (2010).
- [49] J. Heyd and G. E. Scuseria, Assessment and validation of a screened Coulomb hybrid density functional, *J. Chem. Phys.* **120**, 7274 (2004).
- [50] J. Heyd, J. E. Peralta, G. E. Scuseria, and R. L. Martin, Energy band gaps and lattice parameters evaluated with the Heyd-Scuseria-Ernzerhof screened hybrid functional, *J. Chem. Phys.* **123**, 174101 (2005).
- [51] J. Paier, M. Marsman, K. Hummer, G. Kresse, I. C. Gerber, and J. G. Ángyán, Screened hybrid density functionals applied to solids, *J. Chem. Phys.* **124**, 154709 (2006).
- [52] A. A. Mostofi, J. R. Yates, Y. S. Lee, I. Souza, D. Vanderbilt, and N. Marzari, Wannier90: A tool for obtaining maximally-localised wannier functions, *Comput. Phys. Commun.* **178**, 685 (2008).